Narrow-area Bragg-edge transmission of iron samples using superconducting neutron sensor

The Dang Vu[1,2], Hiroaki Shishido[3,4], Kazuya Aizawa[2], Takayuki Oku[2], Kenichi Oikawa[2], Masahide Harada[2], Kenji M. Kojima[4,5], Shigeyuki Miyajima[6], Kazuhiko Soyama[2], Tomio Koyama[4], Mutsuo Hidaka[7], Soh Y. Suzuki[8], Manobu M. Tanaka[9], Alex Malins[10], Masahiko Machida[10] and Takekazu Ishida[1,4]

[1]Division of Quantum and Radiation Engineering, Osaka Prefecture University, Sakai, Osaka 599-8570, Japan
[2]Materials and Life Science Division, J-PARC Center, Japan Atomic Energy Agency, Tokai, Ibaraki 319-1195, Japan
[3]Department of Physics and Electronics, Graduate School of Engineering, Osaka Prefecture University, Sakai, Osaka 599-8531, Japan
[4]NanoSquare Research Institute, Osaka Prefecture University, Sakai, Osaka 599-8570, Japan
[5]Centre for Molecular and Materials Science, TRIUMF, 4004 Wesbrook Mall, Vancouver, BC V6T 2A3, Canada
[6]Advanced ICT Research Institute, National Institute of Information and Communications Technology, 588-2 Iwaoka, Nishi-ku, Kobe, Hyogo 651-2492, Japan
[7]Advanced Industrial Science and Technology, Tsukuba, Ibaraki 305-8568, Japan
[8]Computing Research Center, Applied Research Laboratory, High Energy Accelerator Research Organization (KEK), Tsukuba, Ibaraki 305-0801, Japan
[9]Institute of Particle and Nuclear Studies, High Energy Accelerator Research Organization (KEK), Tsukuba, Ibaraki 305-0801, Japan
[10]Center for Computational Science & e-Systems, Japan Atomic Energy Agency, 178-4-4 Wakashiba, Kashiwa, Chiba 277-0871, Japan.

E-mail: vuthedang@omu.ac.jp

Abstract. This study investigates a current-biased kinetic inductance detector (CB-KID) performance by investigating Bragg-edge spectra from the restricted-area neuron transmission of materials. Iron samples with a size of $5 \times 5 \times 2$ mm^3 were used as typical test materials. The ergodic theorem was used to obtain a visible transmission spectrum so that a long-time averaging of a transmission spectrum can alternatively be evaluated using a space average of independently selected area spectra with the same ensemble size. The most visible edges were observed with a limited area sample of 0.43 mm^2 using a minimum time bin of 25 μs in a time-of-flight (ToF) spectrum or a wavelength resolution of 0.0007 nm of each neutron pulse at beamline BL10 of the Japan Proton Accelerator Research Complex (J-PARC) center. The main Bragg edge of iron as a sum of random 100 ensembles (with an ensemble size of 3.1×2.3 μm^2) thus obtained has a distinctive signal-to-noise ratio and can be fitted well with the Rietveld Imaging of Transmission Spectra (RITS) program with Miller indices. We consider that our CB-KID system is, in principle, able to analyze the Bragg edge of samples as small as 3.1×2.3 μm^2.

1. Introduction

Since neutrons directly interact with nuclei instead of the electron cloud of constituent elements, they have a different characteristic compared with X-ray and other probes [1]. As a matter of fact, substances become visible with neutron beams even though it is almost impossible to see them using X-ray and gamma-ray imaging techniques. A neutron imaging technique provides a useful means of investigating test samples. Moreover, in an energy-dispersive analysis, various material properties are investigated with the aid of the wave nature of neutron beams. Intense pulsed neutrons are powerful in efficiently obtaining wavelength-sensitive properties of substances together with the time-of-flight (ToF) method. Therefore, neutron beams have been recognized as one of the most powerful tools for conducting the nondestructive inspection of a wide range of materials [2]. A neutron detector has three important parameters in the application of neutrons in material science, i.e., spatial resolution, neutron detection efficiency, and energy resolution. We first proposed the idea of a superconducting neutron sensor called a current-biased kinetic inductance detector (CB-KID) [3] and recently reported systematic investigations on its characteristics to optimize the operating conditions [4,5]. We can improve the detection efficiency of the detector by increasing the operating temperature of the superconducting detector to a critical temperature [6]. A delay-line technique of the four-terminal CB-KID successfully achieved neutron imaging with a spatial resolution of 16 μm [5]. We observed neutron transmission images of practical Gd islands with various sizes and thicknesses with CB-KID and demonstrated that the neutron transmission images of various Gd islands were in good agreement with the scanning electron microscope (SEM) images [7]. Since thermal and cold neutrons behave like waves, they inform the wavelength-sensitive interference properties of materials through the Bragg diffraction, i.e., the Bragg edges in the neutron transmission spectra can be observed by coherent scattering in crystalline materials. This enables us to conduct nondestructive studies of phase, texture, and residual stress in the test materials [8,9]. Table 1 presents a comparison of the specifications of three different neutron detectors, namely, CB-KID, microchannel plate (MCP) detector [10], and micropixel chamber-based neutron imaging detector (μNID) [11]. Scintillation-type neutron detectors are widely used, and good review articles are available [12,13].

Table 1. Comparison of three different neutron detectors, i.e., current-biased kinetic inductance detector (CB-KID), microchannel plates (MCPs), and micropixel chamber-based neutron imaging detector (μNID) in several specifications, i.e., operating principle, temporal resolution, sensing area, efficiency for thermal neutrons and spatial resolution. Cited values are not the best but representative (see references).

	CB-KID [5,6,7]	**MCPs** [10]	**μNID** [11]
Operating principle	Superconducting meanderlines	Microchannel plates	Micropatterned electrode
Temporal resolution	1 ns	1 μs	0.25 μs
Sensing area	15x15 mm^2	14x14 mm^2	100x100 mm^2
Efficiency (at 25.3 meV)	1%	78%	26%
Spatial resolution	16 μm	55 μm	0.1mm

This work investigates the Bragg edges in the neutron transmission spectra from restricted areas of the test samples to show the energy-selective wave nature of the materials with our superconducting sensor. For this study, we used an iron test sample because it provides visible Bragg edges with assigned Miller indices as a wavelength function. We analyzed neutron images of the test sample using the ToF method with a time bin of 25 μs (or a wavelength resolution of 0.0007 nm) of each neutron pulse. This study aimed to answer how narrow we can select a testing area for a sample to recover the Bragg edges using our high-resolution superconducting neutron sensor. We systematically investigated the size of the testing area from a few millimeters square to a restricted area of $3.1 \times 2.3\ \mu m^2$. Lack of statistics in neutron transmission intensity is crucial in the investigation of a restricted area as it is a trade-off relation between the arriving neutron intensity and the analyzing area size under the condition of fixed neutron flux intensity. Thus, we attempted to realize transmission spectra with good statistics to replace a long-time average spectrum with an ensemble-averaged spectrum based on the ergodic theorem [14]. We performed an ensemble averaging of randomly selected test areas with identical sizes (average pixel size of $3.1 \times 2.3\ \mu m^2$) to obtain a visible transmission spectrum. We discuss the potential capabilities of the CB-KID sensor in treating fine structural features of various materials when the neutron intensity increases drastically to be available for researchers in the future.

2. Experimental details

2.1. Superconducting Neutron Sensor

One of the best superconducting neutron sensors was used for this experiment. The characteristics of the sensor were systematically investigated in a previous study [4,6]. The structure of a superconducting neutron sensor consists of a pair of meanderlines (X and Y sensors) [15–17] with an orthogonal stacking and a ^{10}B layer deposited on top of the X and Y meanderlines to convert neutrons into charged particles to make it easier to sense an electroneutral particle. The sensitive area of the sensor used was 15 × 15 mm. The nanowire width of the X (or Y) Nb meanderline was 900 nm, and the space between two neighboring nanowire segments was 600 nm. These values gave a 1.5-μm repetition period with 10,000 repetitions to reach an effective width of 15 mm and a total length ℓ of 151 m of the meanderline. These components were stacked in a thermally oxidized Si substrate with eight layers from the bottom: (1) 300-nm-thick SiO_2, (2) 300-nm-thick Nb ground plane, (3) 350-nm-thick SiO_2 layer, (4) 50-nm-thick Nb Y meanderline, (5) 150-nm-thick SiO_2 layer, (6) 50-nm-thick Nb X meanderline, (7) 50-nm-thick SiO_2 layer, and (8) 70-nm ^{10}B neutron conversion layer on top of the CB-KID. The superconducting neutron sensor used in this study was designed using a computer-aided design software (LayoutEditor) to fabricate the device at the clean room for analog-digital superconductivity (CRAVITY) at the National Institute of Advanced Industrial Science and Technology (AIST).

2.2. Measurement System

Figure 1 presents the schematic of the measurement system used with CB-KID. To refrigerate the superconducting neutron sensor down to an operating temperature of 7.9 K, the neutron sensor and test samples were installed on an antivibration cold stage of a Gifford–McMahon (GM) refrigerator. Long-time measurements of CB-KID were performed at a stable cryogenic temperature without feeding liquid helium. The temperature of the superconducting sensor was controlled and monitored using two temperature controllers (Cryocon Model 44) with electric resistance heaters and Cernox thermometers, installed around the neutron sensor and the cold stage of the GM refrigerator with a LabVIEW program. The X and Y meanderlines were fed with direct current (DC) bias currents in series with two DC adjustable voltage sources and bias resistors. Four voltage signals from a single neutron event on the meanderlines were amplified using low-noise amplifiers (NF SA-430F5), and they were divided by four splitters to input both a 32-channel time-to-digital converter (TDC) module for the Kalliope-DC readout circuit [18] and a four-channel 2.5-GHz sampling digital oscilloscope (Teledyne LeCroy HDO4104-MS). The former has a time resolution of 1 ns, whereas the latter has 0.4 ns. The alternating current (AC) power supplied to the above instruments was provided by two stabilized AC power sources (NF EC1000SA) to avoid notable environmental noises provided through the AC power line of the large-scale facility. The amplitudes of neutron signals were tuned by adjusting the amplitudes of the bias currents to the X and Y meanderlines while monitoring them by the high-speed digital oscilloscope under irradiation of neutron beams to the superconducting neutron sensors at a cryogenic operating temperature. Subsequently, the signal amplitudes of the four channels were adjusted by setting the 16-bit variable attenuators (ATT, Hoshin Electronics N032) placed in front of the TDC inputs of the Kalliope-DC readout circuit. Semirigid cables (50 Ω), microminiature coaxial (MMCX) connectors, and subminiature version A (SMA) connectors were used to transmit a high-frequency signal pulse from the cryogenic temperature CB-KID to the room temperature readout instruments inside the cryostat to reduce noises. Neutron irradiation was performed for 141 h under a proton power of 502 kW at the J-PARC to obtain the transmission images and transmission spectra of the test samples.

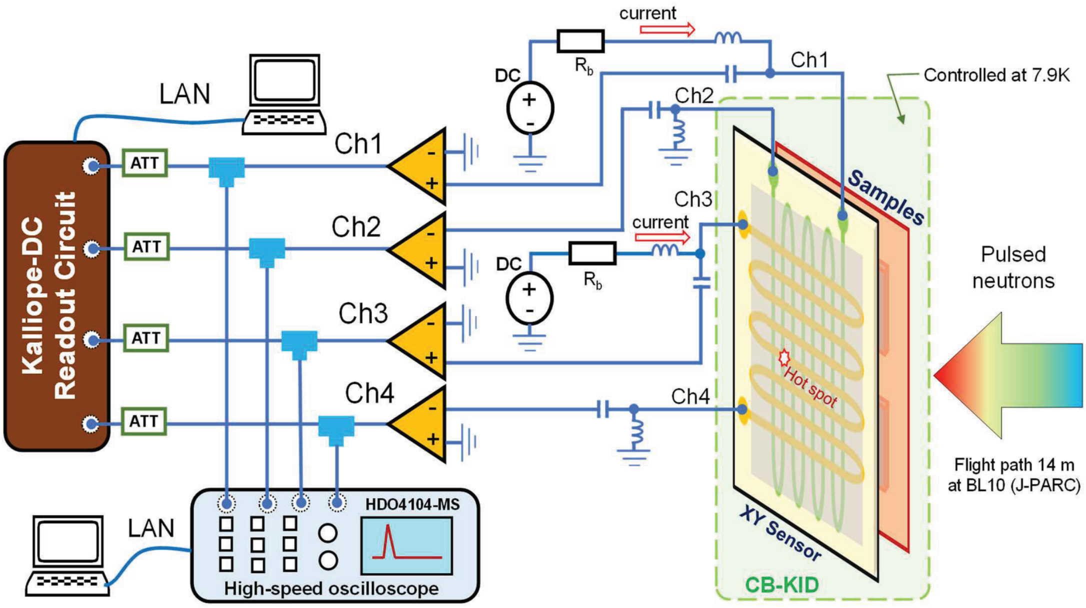

Figure 1. Schematic diagram of the superconducting neutron imaging system. Pulsed neutrons were incident on the substrate side of CB-KID after passing through the test samples through the 14-m long beam-line (BL10) of Material and Life Science Experimental Facility (MLF) at J-PARC. The detector and samples were cooled down to a cryogenic temperature at 7.9 K using a Gifford–McMahon cryocooler. The neutron detector consists of the X and Y-meanderlines and a ^{10}B neutron conversion layer. Neutron signals arising from both ends of the two meanderlines were amplified by ultra-low noise amplifiers to feed into a Kalliope-DC readout circuit via adjustable attenuators (ATT) and an oscilloscope. The system was controlled by two computers for the Kalliope readout circuit and the oscilloscope connected with local area network (LAN) cables.

2.3. Test Samples

Four test samples (5 × 5 mm, 2 mm in thickness) of iron-containing 0.13 wt.% of C were prepared, containing 0.21 wt.% of Si, 1.44 wt.% of Mn, 0.56 wt.% of Mo, and 0.02 wt.% of Nb as impurities. Although the impurities contained were not for this study but for other purposes, such as probing nuclear resonance absorption dips in neutron transmission spectra at higher neutron energies, which have little effect in observing the Bragg edges from iron samples. These samples were fixed with a tiny drop of epoxy adhesive on a 0.1-mm-thick Al plate. Figure 2(a) presents an optical photo of these samples (B1, B2, B3, and B4) on the Al plate, where black lines and a red dot were drawn using a marker ink to discriminate the sample position. The samples on the Al plate were then placed on an Al alloy mount with a milling hole of 13 × 13 mm with a 3.7-mm depth. Finally, the Al plate was located at a 0.7-mm distance from the CB-KID meanderlines. The iron samples were cooled down to the CB-KID temperature to place them at a 0.8-mm distance from the CB-KID sensor. A neutron transmission experiment was conducted at beamline BL10 in the J-PARC, where the pulsed neutrons were used at a 25-Hz repetition employing the ToF method at the beamline and length of 14 m. Neutron transmission imaging with high spatial resolution and wavelength (λ)-sensitive transmission spectroscopy, such as a Bragg-edge transmission with a wavelength resolution of $\Delta\lambda/\lambda = 0.33\%$, were conducted [19].

3. Results and discussion

This work intends to answer how narrow we can select a testing area with a visible Bragg edge using a high-spatial-resolution neutron sensor. The characteristics of iron in a neutron transmission have been thoroughly established in both experiments and simulations [2,20], where multiple Bragg edges appear in a wide range of wavelengths rather visibly shorter than 0.4 nm. Therefore, an iron sample was considered to be a good candidate as a test material for examining the CB-KID performance for revealing the Bragg-edge spectra manifested from a transmission spectrum by selecting a restricted area of materials.

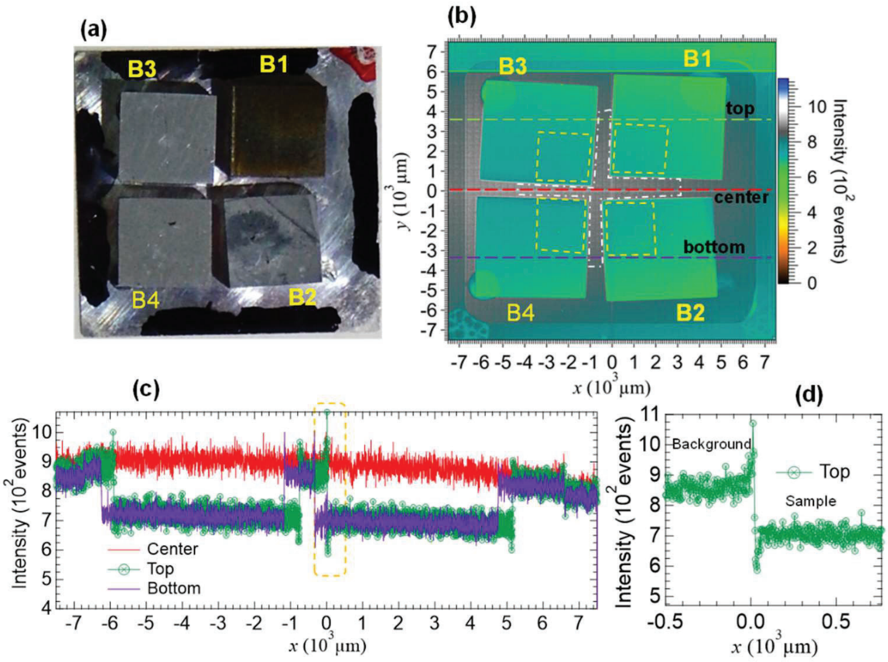

Figure 2. **(a)** Optical photo of four iron test samples (B1, B2, B3, B4) used for the present study. Samples were fixed on the 0.1-mm thick Al plate mounted on an Al-alloy sample mount. **(b)** Neutron transmission image of iron test samples (B1, B2, B3, B4). **(c)** Horizontal line profiles correspond to the top (in green), center (in red) and bottom (in violet) positions in neutron image; **(d)** A zoomed line profile of neutron transmission near the left-hand-side edge of test sample B2. This explains an enhanced contrast of the images at the sample edge.

Figure 2(b) presents the neutron transmission images, where four test samples (B1, B2, B3, and B4) clearly appeared at the corresponding positions of samples in figure 2(a). Furthermore, it is evident that the appearance of epoxy resin was used to fix the iron sample at a corner under the sample (at a sample corner close to the corner of the Al plate). It can be noted that resin adhesives were not so visible in the photo (see figure 2(a)) because they were located under the 2-mm-thick iron samples. On the contrary, the black lines at the four sides and red dots at the corner of figure 2(a) did not appear in figure 2(b). However, the 13 × 13-mm milling hole of the Al alloy mount can be seen in figure 2(b). This is due to a difference in the Al alloy thickness present and the diffraction/reflection edge effect (see below). The appearance of an image contrast above $y > 6$ mm indicates the existence of defect(s) in the superconducting sensor. This indication is a characteristic feature of neutron beams in probing samples compared with optical observations. After careful inspection of the neutron image in figure 2(b), it can be seen that the contrast in neutron intensity at the borders of the samples is somewhat exaggerated in neutron transmission images compared with other parts of the iron samples. To highlight the intensity contrast, we took the horizontal line profiles (see figure 2(c)) at the three different positions: the upper side (along a yellow dashed line in figure 2(b)), the central area (along a red dashed line in figure 2(b)), and the bottom side (along a blue dashed line in figure 2(b)). Negative peaking was present in the neutron intensity at the sample side and positive peaking at the empty side (background-area side). These phenomena are explained by the refraction/reflection and scattering of neutron beams at the sample edges when neutron beams arrive at the test samples in a way that is highly parallel to their surfaces. However, when neutron beams propagate from vacuum to iron along the flat surface area of the sample, refraction/reflection may force back neutron beams from the inside of the iron sample to the vacuum environment. These phenomena should occur at the four horizontal surfaces of each iron sample. Therefore, positive and negative peakings occur in the line profiles in figure 2(c). The dashed-line area in figure 2(c) is zoomed in figure 2(d) to explain the phenomena more clearly. Before this study, Tremsin *et al.* [21] reported similar phenomena in neutron imaging. The negative and positive peakings were disturbing with regard to the purpose of this study, but we only focused on the neutron transmission spectrum inside the samples in our analyses.

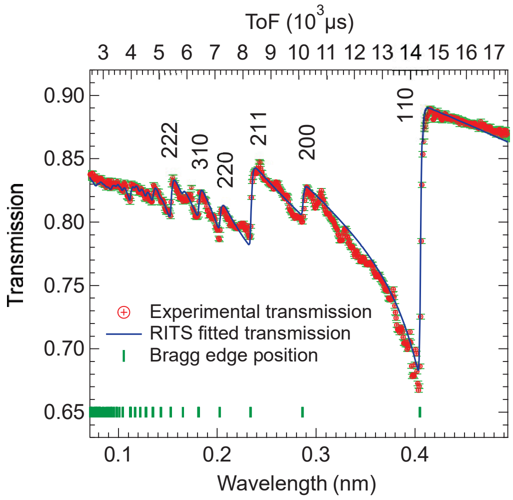

Figure 3. A typical neutron transmission spectrum of the iron sample obtained by the present experiment. The transmission was calculated by the ratio of sum spectrum of four sample areas (indicated by yellow dashed-line areas of 23.64 mm^2 in figure 2(b)) and the spectrum of the background area (indicated by a white dot-and-dash-line area of 10.68 mm^2 in figure 2(b)) for the purpose of reducing a difference in sampling areas. Most of typical Bragg edges of the iron samples can clearly be identified by eyes in the wavelength range from 0.1 nm to 0.45 nm. The transmission spectrum fitted with RITS code was overlaid on red data points as a blue solid line.

We discuss the Bragg-edge profile in the neutron transmission spectra of the iron samples. Figure 3 presents a typical neutron transmission of the sample in a wide area of 23.64 mm^2, which is wide enough and almost the same as that of the single sample. The transmission was calculated by taking the ratio of the neutron intensity in the sample area, which is indicated by the dashed yellow lines in figure 2(b) and the intensity in the area without the iron samples (denoted as the background area) indicated by the white dot and dashed line in figure 2(b). The procedure for taking the ratio between the sample and background areas was helpful in compensating for the differences in the beam intensities as wavelength functions. The neutron transmission data in this study were analyzed using the ToF method from 25 μs to 20 ms or a wavelength of 0.0007 to 0.57 nm in a time bin of 25 μs, giving the best wavelength resolution of 0.0007 nm [19]. A neutron image was constructed with a resolution of an area of elementary pixel size (x and y direction size of 3.1×2.3 μm^2). We found that the experimental transmission had good statistics to be able to see most of the typical Bragg edges in the wavelength of 0.15 to 0.4 nm. Figure 3 presents the transmission of the iron samples evaluated as a function of wavelength or ToF. Many steps can be seen in the experimental spectrum in this figure. We performed fitting of the experimental spectrum using a RITS program [20], where the major Miller indices of 110, 200, 211, 220, 310, and 222 were labeled in the transmission spectrum of the iron samples (see figure 3). We confirmed that the experimental transmission spectrum was in good agreement with the simulation spectrum obtained from the RITS code.

The superconducting neutron sensor in this study exhibited a high spatial resolution [5,7]. This study aimed to determine how narrow we can select a testing area to obtain a visible Bragg edge using an iron test sample with CB-KID. There was a trade-off relation between the choice of the measurement area and time. Although the capability of the facility limits the neutron flux density, it was unrealistic to be assigned a very long beam time in any available facilities. The ensemble average equals the time average from the ergodic theorem in statistical mechanics [14]. In other words, a sufficiently large collection of random ensembles from a sample system can represent the average statistical properties of the entire process of an isolated small ensemble. The long-time averaged behavior of the narrow area of the test sample was examined by considering an ensemble average over many identical ensembles randomly selected from the inside of the test sample.

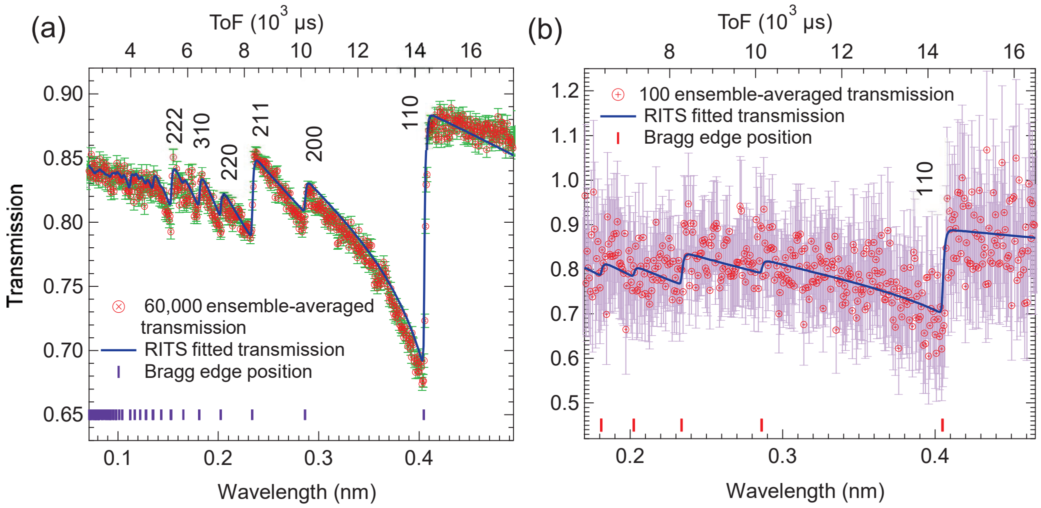

Figure 4. (a) Neutron transmission spectrum of iron test samples obtained by using a limited area of 0.43 mm^2 in total with summing randomly-chosen 60,000-pixel ensembles from the sample area. The transmission spectrum shows a good signal-to-noise ratio while error bars and a blue fitting curve are shown in the figure. This is almost identical with features of the visible Bragg edges obtained by using a wider-sample area 23.64 mm^2 as showed in figure 2(b). (b) The experimental transmission spectrum composed from randomly-chosen 100 pixels (713 μm^2 in total). Although a signal-to-noise ratio in red data points is moderate, a blue RITS fitting curve is shown. The major Bragg edge at around 0.4 nm can be discernably recognized.

To reveal the minimum size of the sample area enough for visualizing Bragg edges in the transmission spectra, the main 110 Bragg edge was particularly important in the discussion of this issue. For this purpose, based on the ergodic theorem [14], we took an ensemble average for several ensembles, of which the area was randomly taken from the inside of the test samples to evaluate the transmission spectrum of each area. This yielded a virtual transmission spectrum that could be obtained by conducting a very long-time average of the transmission spectrum through a single narrow ensemble area of the test samples. The space average of independently selected area spectra with the same ensemble size can be evaluated. Figure 4(a) presents a neutron transmission spectrum of the iron test sample in a restricted area, which was obtained by summing up the spectra from randomly chosen 60,000 pixels of the 3.1 × 2.3 μm^2 area from the test sample area. We observed that the total area consisting of the 60,000 ensembles was considerably smaller than the sample size. Furthermore, we carefully removed the ensemble case whenever the selected area overlapped with the areas of other ensembles in choosing randomly chosen ensembles in analyses. This ensures that any area can be independent with each other so that the ergodic theorem can be applied appropriately. The same number of constituent pixels from the background area (outside the test iron samples) from close locations to the test samples were used. We found that the signal-to-noise ratio was not so good as in the transmission spectrum obtained from the wider area in figure 3, but it was good enough to discriminate several different Bragg edges in the spectrum (see labels in figure 4(a)). We concluded that all Bragg edges are still clearly visible, even employing the restricted area of 0.43 mm^2. This conclusion would become important as it is, in principle, possible to obtain the Bragg-edge profile for a small restricted area of a test material when we use a high-spatial-resolution neutron sensor with plenty of long beam time.

We further attempted to reduce the number of ensemble pixels for studying the minimum area to obtain a neutron transmission spectrum with the discernible main Bragg edge exhibiting a reasonable signal-to-noise ratio. This attempt helped estimate the data acquisition time to obtain a discernible Bragg edge within the limitation of beam-time allocation in actual planning. Figure 4(b) presents the neutron transmission spectrum obtained with 100 ensembles (713 μm^2 in total area) with error bars, in which we noticed that the signal-to-noise ratio was not so good compared with that in figure 4(a). However, the eye still clearly identified the main Bragg edge (110) in figure 4(b), where it was helpful to overlay the transmission spectrum obtained by fitting with the RITS program on the experimental data. We ensured that all analyses in this study were conducted using raw-spectrum data; however, the signal-to-noise ratio can be improved by averaging over serval pixels image or averaging over a time bin in the ToF spectrum. We interpret that this is the minimum area size (3.1×2.3 μm^2) at which a visible Bragg edge can be obtained if a beam time is available hundred times longer than the present measurements. Our sensor is suitable to study the properties of the material with a size larger than 31×23 μm^2 (10×10 pixels) with the beam time of the present study. Regarding the wavelength resolution, Tremsin *et al.* [10] observed the neutron transmission of an Al cylinder with a diameter of 50 mm; they conducted this observation by using an MCP neutron detector with a 14×14 mm^2 sensitive area with the Timepix readout. They succeeded in observing a neutron transmission spectrum with main Bragg-edge in an area of 165×165 μm^2 (3×3 pixels) with a minimum of wavelength bin of 0.0004 nm. The spectra were built with 55-μm shifts, which is one-third of the averaging width.

4. Summary

It is a reasonable hypothesis that a high-spatial-resolution Bragg-edge analysis is possible if a high-spatial-resolution neutron detector is used. To confirm this hypothesis, we analyzed neutron transmission spectra with a restricted area down to spatial resolution (3.1×2.3 μm^2) and a minimal wavelength window (0.0007 nm). This is to determine the minimum area size required for recovering clear Bragg edges of the 2-mm-thick iron test samples using our superconducting neutron sensor. Instead of very long-time measurements required to achieve transmission spectra with good statistics, we performed ensemble averaging of the transmission spectra of randomly chosen restricted areas based on the ergodic theorem. The multiple Bragg edges of the iron test samples were nicely reproduced *via* ensemble averaging of 60,000 identical ensembles with an area size of 3.1×2.3 μm^2, where the analyzed area reached 0.43 mm^2 in total within the test samples. As a reference, we demonstrated a clear neutron transmission spectrum with a single wider area of 23.64 mm^2 of the test samples. We found that our sensor can still detect the main 110 Bragg edge of iron beyond the noise floor even when the number of ensembles was limited to 100 with the smallest ensemble size (3.1×2.3 μm^2). Several visible edges clearly appeared, with a total sample size of 0.43 mm^2 as a sum of all ensembles. These Bragg edges were visible with a good signal-to-noise ratio. The Miller indices were assigned well with the RITS program [20]. This was useful to estimate the required beam time to obtain a visible transmission spectrum with a long data acquisition time. We simulated a transmission spectrum using the RITS program to compare it with the experimental neutron transmission spectrum. It can be concluded that a high-spatial-resolution Bragg edge analysis can be conducted using our superconducting neutron sensor. Our finding would be more important when a neutron source becomes much more intense by three orders of magnitude in the field of inertial fusion energy facilities in the future [22].

Acknowledgment

The authors are grateful to Y. Su for her kind suggestions for using the RITS program to fit our experimental neutron transmission spectra. This work is partially supported by Grant-in-Aid for

Scientific Research (Nos. JP16H02450, JP21H04666, JP21K14566) from Japan Society for the Promotion of Science (JSPS) and the project program of MLF (Nos. 2018P0201, 2021P0501).

References

[1] Tengattini A, Lenoir N, Andò E and Viggiani G 2021 Neutron imaging for geomechanics: A review *Geomech. Energy Environ.* **27** 100206
[2] Kardjilov N, Manke I, Woracek R, Hilger A and Banhart J 2018 Advances in neutron imaging *Mater. Today* **21** 652–72
[3] Ishida T, Yoshioka N, Narukami Y, Shishido H, Miyajima S, Fujimaki A, Miki S, Wang Z and Hidaka M 2014 Toward mega-pixel neutron imager using current-biased kinetic inductance detectors of Nb nanowires with ^{10}B converter *Journal of Low Temperature Physics* **176** 216–221
[4] Vu T D *et al*. 2019 Temperature dependent characteristics of neutron signals from a current-biased Nb nanowire detector with ^{10}B converter *Journal of Physics: Conference Series* **1293** 012051
[5] Iizawa Y, Shishido H, Nishimura K, Vu T D, Kojima K M, Koyama T, Oikawa K, Harada M, Miyajima S, Hidaka M, Oku T, Soyama K, Aizawa K, Suzuki S Y and Ishida T 2019 Energy-resolved neutron imaging with high-spatial resolution using a superconducting delay-line kinetic inductance detector *Supercond. Sci. Technol.* **32** 125009
[6] Vu T D *et al*. 2020 Kinetic inductance neutron detector operated at near critical temperature *Journal of Physics: Conference Series* **1590** 012036
[7] Vu T D *et al.* 2021 Practical tests of neutron transmission imaging with a superconducting kinetic-inductance sensor *Nucl. Instrum. Meth. Phys. Res. A* **1006** 165411
[8] Santisteban J R, Edwards L, Steuwer A and Withers P J 2001 Time-of-flight neutron transmission diffraction *J. Appl. Cryst* **34** 289–97
[9] Steuwer A, Withers P J, Santisteban J R and Edwards L 2005 Using pulsed neutron transmission for crystalline phase imaging and analysis *J. Appl. Phys.* **97** 074903
[10] Tremsin A S, McPhate J B, Kockelmann W, Vallerga J V., Siegmund O H W and Feller W B 2011 High resolution Bragg edge transmission spectroscopy at pulsed neutron sources: Proof of principle experiments with a neutron counting MCP detector *Nucl. Instrum. Meth. Phys. Res. A* **633** S235–S238
[11] Shinohara T *et al.* 2020 Development of Energy-Resolved Neutron Imaging Detectors at RADEN *Rev. Sci. Instrum.* **91** 043302
[12] Rhodes N J 2006 Scientific Reviews: Status and Future Development of Neutron Scintillation Detectors *Neutron News* **17**:1 16-18
[13] Rhodes N J 2012 Scintillation detectors *Neutron News* **23**:4 26-30
[14] Moore C C 2015 Ergodic theorem, ergodic theory, and statistical mechanics *Proc. Natl. Acad. Sci. U. S. A.* **112** 1907–11
[15] Ishida T *et al.* 2008 Superconducting MgB_2 thin film detector for neutrons *J. Low Temp. Phys.* **151** 1074–1079
[16] Shishido H, Miyajima S, Narukami Y, Oikawa K, Harada M, Oku T, Arai M, Hidaka M, Fujimaki A and Ishida T 2015 Neutron detection using a current biased kinetic inductance detector *Appl. Phys. Lett.* **107** 232601
[17] Yoshioka N, Yagi I, Shishido H, Yotsuya T, Miyajima S, Fujimaki A, Miki S, Wang Z and Ishida T 2013 Current-biased kinetic inductance detector using MgB_2 nanowires for detecting neutrons *IEEE Trans. Appl. Supercond.* **23** 2400604
[18] Kojima K M *et al.* 2014 New μSR spectrometer at J-PARC MUSE based on Kalliope detectors *Journal of Physics: Conference Series* **551** 012063
[19] Oikawa K *et al.* 2008 Design and application of NOBORU-NeutrOn Beam line for Observation and Research Use at J-PARC *Nucl. Instrum. Meth. Phys. Res. A* **589** 310–317
[20] Sato H 2018 Deriving quantitative crystallographic information from the wavelength-resolved neutron transmission analysis performed in imaging mode *J. Imaging* **4** 7
[21] Tremsin A S, Lehmann E H, Kardjilov N, Strobl M, Manke I, McPhate J B, Vallerga J V, Siegmund O H W and Feller W B 2012 Refraction contrast imaging and edge effects in neutron radiography *J. Instrum.* **7** C02047
[22] Taylor A, Dunne M, Bennington S, Ansell S, Gardner I, Norreys P, Broome T, Findlay D and Nelmes R 2007 A Route to the Brightest Possible Neutron Source? *Science* **315** 1092–1095